aerospace

MDPI

Article

High-Resolution Wavenumber Bandpass Filtering of Guided Ultrasonic Wavefield for the Visualization of Subtle Structural Flaws

Lee Shi Yn [1], Fairuz Izzuddin Romli [1], Norkhairunnisa Mazlan [1], Jung-Ryul Lee [2], Mohammad Yazdi Harmin [1,*] and Chia Chen Ciang [2,*]

[1] Department of Aerospace Engineering, Universiti Putra Malaysia, Serdang 43400, Selangor, Malaysia
[2] Department of Aerospace Engineering, KAIST, Daejeon 34141, Republic of Korea
* Correspondence: myazdi@upm.edu.my (M.Y.H.); chiacc@kaist.ac.kr (C.C.C.)

Abstract: Guided ultrasonic wavefield propagation imaging (GUPI) is useful for visualizing hidden flaws in aerospace thin-walled structures, but the need for subjective signal processing involving three-dimensional Fourier transformation to increase the visibility of subtle flaws hinders its wider acceptance. A high-resolution wavenumber bandpass filter capable of consolidating subtle flaw-relevant information from a wide frequency band using only two-dimensional Fourier transformation was proposed. The filter overturns the long-standing belief that modes must be separated based on narrow-band data acquisition or processing to achieve high flaw visibility. Its characteristics and advantages were experimentally demonstrated through enhanced visualization of hidden wall-thinning flaws of a plate specimen. Its strength was further demonstrated through the first GUPI visualization of a partially loosened bolt, with unprecedented clarity to discern bolt tightness levels. The results conclusively proved that the proposed filter significantly enhances the resolution of GUPI within a structured processing framework.

Keywords: aerospace structures; laser ultrasound imaging; Lamb's waves; wavefield propagation imaging; nondestructive testing; features extraction; wall thinning; fastener loosening

Citation: Lee, S.Y; Romli, F.I.; Mazlan, N.; Lee, J.-R.; Harmin, M.Y.; Chia, C.C. High-Resolution Wavenumber Bandpass Filtering of Guided Ultrasonic Wavefield for the Visualization of Subtle Structural Flaws. *Aerospace* **2024**, *11*, 524. https://doi.org/10.3390/aerospace11070524

Academic Editor: Sebastian Heimbs

Received: 21 May 2024
Revised: 18 June 2024
Accepted: 24 June 2024
Published: 27 June 2024

1. Introduction

Guided ultrasonic wavefield propagation imaging (GUPI) [1–3] is an emerging nondestructive testing (NDT) method being used for the detection and evaluation of hidden defects in thin-walled structures using Lamb waves [4,5]. It is particularly important for the inspection of aerospace structures because thin-walled structural parts are commonly found in this field due to advancements in structural, material, and design optimizations [6–10]. It offers numerous advantages, including the ability to achieve high detectability by selecting suitable Lamb wave frequencies and modes for imaging [11–13]. Conventionally, frequency bandpass filtering is employed due to the availability of standard filters. However, frequency filtering is an indirect approach because, for all frequency ranges, there are at least two fundamental Lamb wave modes, even for an undamaged isotropic thin plate. Consequently, these wave modes interfere with each other and compromise the imaging quality. A more direct approach is to generate and measure only one suitable wave mode. However, single-mode transduction often necessitates theoretical or numerical analysis of the structural material [14,15], followed by customization of a transducer or device with adequate mode selectivity. In this context, examples of such innovations include an array or comb transducer with a customized element gap [16,17], an ultrasound-generation laser beam featuring a customized spatial profile [18,19], and a surface-mounted patch designed with a specific spatial pattern [20,21]. Despite their availability and potential, these solutions face limited adoption due to the significant degree of customization required for each inspection.

A more promising alternative is to employ mode filtering after recording the multimodal wavefield. While in some cases involving a limited frequency bandwidth and just two modes in the wavefield, mode filtering can be achieved with a straightforward wavenumber lowpass or highpass filter [22]. The mode filtering becomes challenging when the wavefield comprises more than two modes under some broader conditions, for instance, when examining specimens with local thickness variations, recording wavefields over a wide frequency range, or dealing with specimens of substantial thickness. Under these conditions, a more sophisticated mode filter is needed, and it is being constructed typically in the wavenumber–frequency domain [23–30] as a series of frequency-specific wavenumber bandpasses. However, this approach presents three inherent challenges. Firstly, it necessitates the customized generation of numerous filter windows, each tailored to a discrete frequency instance (i.e., bin) in accordance with the specimen's wavenumber–frequency dispersion curves. Secondly, these dispersion curves are often calculated based on known material properties of the specimen, which can be inaccurate due to variations in environmental conditions [31]. In addition, material property data may be restricted due to proprietary concerns. Alternatively, one can estimate these curves through data-driven models, but this approach is susceptible to potential issues like data quality and model maturity, which can impact estimation accuracy (see Section 3.2.2 in [1] for more details about the estimation of dispersion curves). Lastly, bandpass filtering in the wavenumber–frequency domain is exceptionally time-consuming when applied to large wavefield datasets, especially given the increasing demand for inspecting large structures like the entire aircraft wing. The time requirements can become prohibitive when one must perform three-dimensional (3D) domain transformations for the wavefield data between the space–time domain and the wavenumber–frequency domain, customize a series of filter windows, and estimate the wavenumber–frequency dispersion curves from the measurements within the limited maintenance downtime.

In order to circumvent the inherent challenges, mode filtering in the wavenumber–time domain was explored [32–36]. It is easier to implement from the following perspectives. First of all, only one wavenumber mask is required regardless of the frequency, in contrast to the preparation of multiple frequency-specific wavenumber masks using the conventional method. In addition, the identification of modes is easier using the wavenumber response function [33] due to the possibility of compressing modes' energy into prominent peaks. And lastly, the computation is relatively light due to the transformation of data between the space and wavenumber domains, leaving the time domain untouched.

Despite the advantages, the mode filter falls short in providing a high wavenumber resolution. A high resolution is needed under numerous conditions, especially when the features of interest exist among multiple other modes that have similar wavenumbers. For example, it is needed when isolating the so-called "anomalous waves" [27,28] mode, which is converted from the incident modes by a flaw and often has similar frequency and wavenumber with the incident modes. It is also needed when segregating the wave energy into some narrow wavenumber bins or sub-bands [24,37] for local wavenumber estimation. A narrow band (thus high resolution) wavenumber bandpass filter was constructed in the wavenumber–time domain using a Gaussian-shaped filter mask [38,39] for flaw highlighting. Regrettably, only a vague statement of a "narrow bandwidth" was given without specifying precise information on how narrow it can go. Potential effects or impacts of the window shape have also never been addressed. Moreover, the filter was applied for strictly narrow frequency band data; thus, whether it is suitable for data of broader frequency bands remains unexplored. In addition, some previous applications necessitate the manual selection of one or a few spatial plane(s) of the wavefield data at optimized time instance(s) as input to the filter, which is time-consuming and yields subjective results.

The criticality of accurate wavenumber bandpass filtering, the existence of a knowledge gap concerning the bandwidth and shape of the wavenumber bandpass filter in the wavenumber–time domain, and the need to automate the processing without human intervention for optimization motivate this work. A wavenumber bandpass filter, which

offers an arbitrarily adjustable wavenumber bandwidth, is proposed. Initial results have proved the usefulness of the proposed filter [40], and the results of a more systematic study are presented herein. The contributions of current work include the following: (i) Enabling wavenumber bandpass filtering using two-dimensional (2D) Fourier transformation instead of 3D transformation, thereby reducing the processing time. (ii) Enabling high-resolution wavenumber bandpass filtering down to a single wavenumber bin, thereby significantly improving the wavenumber resolution for more accurate flaws evaluation. (iii) Introducing the notion of "information consolidation" within a wavenumber filtering band, disregarding the frequencies and modes of the wavefield for enhanced detection of subtle anomalies. (iv) Shedding light on the implication of window shape in wavenumber–time domain filtering. (v) Providing a structured framework for wavenumber bandpass filtering without needing any subjective optimization of processing parameters. Lastly, (vi) demonstrating for the first time that the GUPI system can be used to visualize and thereby detect a partially loosened fastener from an image.

The remainder of this paper is structured as follows. The proposed wavenumber bandpass filter is detailed in Section 2, followed by the design of specimens, the descriptions of the data acquisition system, and the experimental setup. The results are given in Section 3, separated into three subsections so that the basic functionality of the proposed filter is validated first, followed by a demonstration of the intrinsic characteristic of the proposed filter, which enables the consolidation or reinforcement of flaw-related information from a broad frequency range disregards of the modes, and finally, how this notion of information consolidation can be harnessed for visualization of a partially loosened fastener. Section 4 provides some additional discussion and clarification on how the proposed filter is distinct from the mode filter and how it can be utilized in a variety of situations. Section 5 presents the concluding remarks and potential future works.

2. Materials and Methods

In this study, a wavenumber bandpass filter is proposed through the reconstruction of the adaptive mode filter described in [33] as a new features-extraction tool that could improve the resolution of the GUPI system. The basic functionality of the proposed filter is first validated through the visualization of hidden flaws in a thin stainless-steel plate. The resolution improvement featured by the proposed filter is demonstrated through the detection and visualization of the partial loosening of a fastener in an aluminum plate. The details of the proposed wavenumber bandpass filter, the specimens with hidden flaws, and the data acquisition steps are given in the following subsections.

2.1. The Proposed Wavenumber Bandpass Filter

The proposed filter features a 2D filter mask that is applied to all sampling time instances of a wavenumber–time domain GUPI data. The overall steps to prepare and apply the filter are shown in Figure 1, where the core components of the filter are highlighted. Other components are not required for the filtration process but can provide optional information to the users for a better understanding of the process. Inputs needed by the filter are shown in red, while intermediate outputs from each process are shown in blue. The description of the filter first covers the core components, followed by descriptions of the optional components.

The wavenumber bandpass filter can be generated according to the steps shown on the right side of the flowchart. To prepare a wavenumber bandpass filter window (mask), suitable values for parameters α, κ_{start}, and κ_{stop}, which, respectively, represent the shape of the filter window, the starting limit of the wavenumber range, and the stopping limit of the wavenumber range, are provided. Arbitrary values can be set depending on the specimen

and processing requirements. Once set, a one-dimensional (1D) filter window with a cosine tapering can be generated in the wavenumber space according to Equation (1):

$$\widetilde{W}_{1D}[\kappa] = \begin{cases} \frac{1}{2}\left\{1 + cos\left[\frac{2\pi}{r}\left(\kappa - \kappa_{start} - \frac{r}{2}\right)\right]\right\} & ; \kappa_{start} \le \kappa \le \kappa_{start} + \frac{r}{2} \\ 1 & ; \kappa_{start} + \frac{r}{2} < \kappa < \kappa_{stop} - \frac{r}{2} \\ \frac{1}{2}\left\{1 + cos\left[\frac{2\pi}{r}\left(\kappa - \kappa_{stop} + \frac{r}{2}\right)\right]\right\} & ; \kappa_{stop} - \frac{r}{2} \le \kappa \le \kappa_{stop} \\ 0 & ; \text{otherwise} \end{cases}, \quad (1)$$

where r represents the ratio of cosine-tapered section length to the bandwidth of the filter, as shown by Equation (2). Parameter α determines the shape of the window within the wavenumber range $\kappa_{start} \le \kappa \le \kappa_{stop}$, such that a Tukey window is generated when $0 < \alpha < 1$; a rectangular window is generated when $\alpha = 0$; and a Hann window is generated when $\alpha = 1$, as shown in Figure 2. This offers high flexibility to suit different bandwidth and weightage requirements, which are discussed later. A 2D filter mask indexed by κ_x and κ_y, which represent the wavenumber in the horizontal and vertical directions, respectively, can then be generated by mapping the elemental values of $\widetilde{W}_{1D}$ into 2D according to Equation (3).

$$r = \alpha\left(\kappa_{stop} - \kappa_{start} + 1\right); \quad 0 \le \alpha \le 1 \quad (2)$$

$$\widetilde{W}_{2D}\left[\kappa_x, \kappa_y\right] = \widetilde{W}_{1D}\left[\sqrt{{\kappa_x}^2 + {\kappa_y}^2}\right] \quad (3)$$

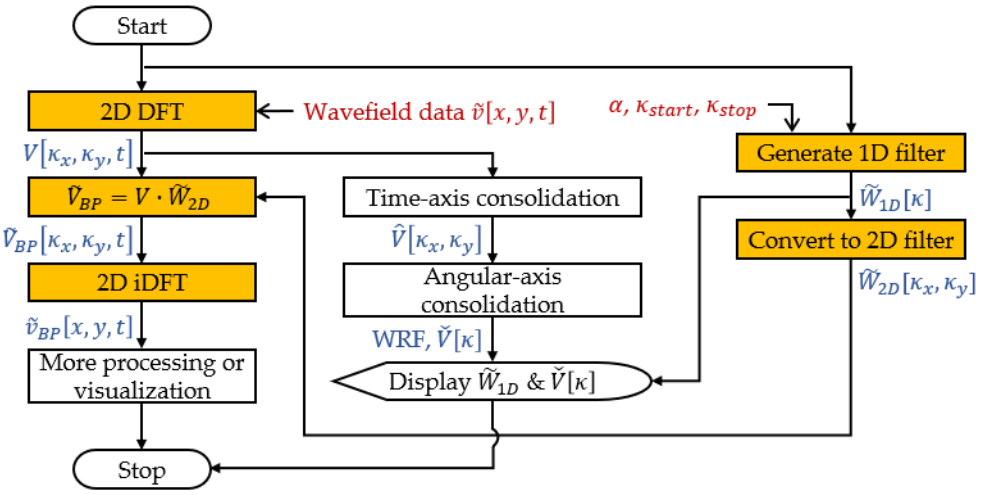

Figure 1. Typical flow of the proposed wavenumber bandpass filter. Core filter components are highlighted. The wavenumber response function (WRF) can be optionally displayed. External inputs are shown in red, while intermediate outputs from each process are shown in blue.

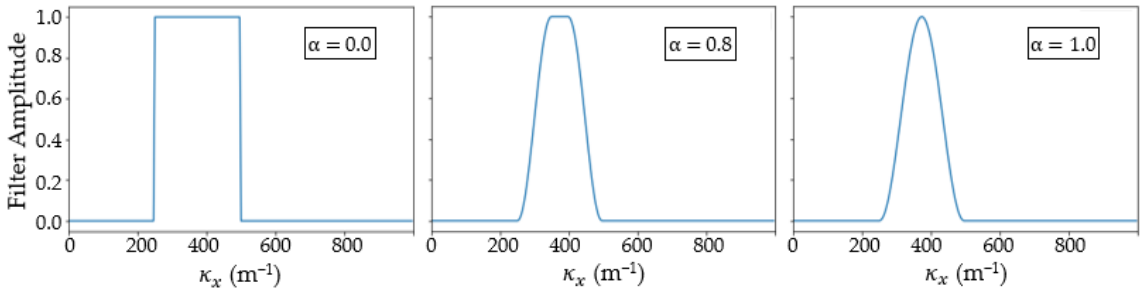

Figure 2. Visualization of 1D filter profiles, plotted using α = 0.0, 0.8, and 1.0, respectively.

The wavenumber bandpass filter can then be applied according to the steps shown at the left of the flowchart given in Figure 1. To do so, consider a set of GUPI space–time domain data $\widetilde{v}[x, y, t]$, which is measured from a thin plate over a spatial domain at positions indexed by $[x, y]$ and along the time domain at instances indexed by t. It is converted into the wavenumber–time domain as $V\left[\kappa_x, \kappa_y, t\right]$ using a 2D discrete Fourier transformation (DFT). The filter window $\widetilde{W}_{2D}\left[\kappa_x, \kappa_y\right]$ can then be applied to the wavenumber–time domain data $V\left[\kappa_x, \kappa_y, t\right]$ through multiplication to each of the t-indexed frames $V\left[\kappa_x, \kappa_y\right]$ according to Equation (4),

$$\widetilde{V}_{BP}\left[\kappa_x, \kappa_y, t\right] = \widetilde{W}_{2D}.V\left[\kappa_x, \kappa_y, t\right], \tag{4}$$

where $\widetilde{V}_{BP}$ represents the wavenumber bandpass filtered data. The $\widetilde{V}_{BP}$ can then be transformed back to the space–time domain as $\widetilde{v}_{BP}[x, y, t]$ using a 2D inversed DFT (iDFT). This wavenumber bandpass filtered data in the space–time domain can either be further processed or presented as a result for flaw visualization. This marks the end of a typical wavenumber bandpass filtering process.

Optional components of the wavenumber bandpass filter, which are located at the center of the flowchart in Figure 1, are now described. As mentioned earlier, these optional components can provide additional information to the users for a better understanding of the filtering process through the visualization of the wavenumber response function (WRF) [33] of a wavefield. To generate a WRF, the wavenumber–time domain data $V\left[\kappa_x, \kappa_y, t\right]$ are consolidated along the time axis into a time-consolidated wavenumber spectrum (TCWS) $\hat{V}\left[\kappa_x, \kappa_y\right]$ according to Equation (5),

$$\hat{V}\left[\kappa_x, \kappa_y\right] = \sum_{t=0}^{T} V\left[\kappa_x, \kappa_y, t\right], \tag{5}$$

where sampling time index t ranges from 0 to T for signals with $(T + 1)$ time samples. The TCWS can be visualized through a contoured plot, in which multiple concentric rings corresponding to the consolidated energy of multiple modes can be identified. The TCWS of a 2 mm thick aluminum plate, energy-normalized and zoomed-in for $\kappa_x, \kappa_y = \pm 400\ \mathrm{m}^{-1}$, is shown in Figure 3a as an example. This TCWS is characterized by two rings over the dark background, in which the inner and outer rings represent the S0 and A0 modes, respectively. Subsequently, by switching to a polar coordinate system with reference to the angle θ defined in Figure 3a, the WRF can be generated according to Equation (6),

$$\check{V}[\kappa] = \sum_{\theta=0}^{2\pi} \hat{V}[\kappa, \theta], \tag{6}$$

where $\kappa = \sqrt{\kappa_x^2 + \kappa_y^2}$ represents radial wavenumber. Note that the corresponding WRF, displayed over a full κ scale up to 1000 m^{-1} in Figure 3b, is characterized by a predominantly flat baseline, with notable peaks at around 50 m^{-1} and 140 m^{-1}. These distinct energy peaks correspond, respectively, to the S0 and A0 modes of the wavefield. The visualization of WRF can potentially provide more information than the TCWS due to additional consolidation of wavefield energy for the exaggerated visual representation of the wavefield modes and sometimes flaw information. The WRF plot serves as a good reference for the users to set suitable filter parameters based on the measured data; thus, the filtering range is typically displayed together with the WRF, as shown by the vertical dashed red lines in Figure 3b. Depending on the preference, a one-dimensional filter window can also be overlaid on the WRF.

The effect of filtering could also be examined by plotting a TCWS and WRF of the filtered data. Just for illustration purposes, applying a $\widetilde{W}_{2D}\left[\kappa_x, \kappa_y\right]$, generated using κ_{start} = 95 m^{-1}, κ_{stop}=185 m^{-1}, and α= 1, as shown in Figure 4, would keep only the A0 mode while discarding all other information, as shown by the filtered TCWS and filtered

WRF in Figure 3c,d, respectively. Please note that the optional components of the filter serve to only provide a visual understanding of the filtering process. The wavenumber bandpass filtering can actually be performed without the optional visualization.

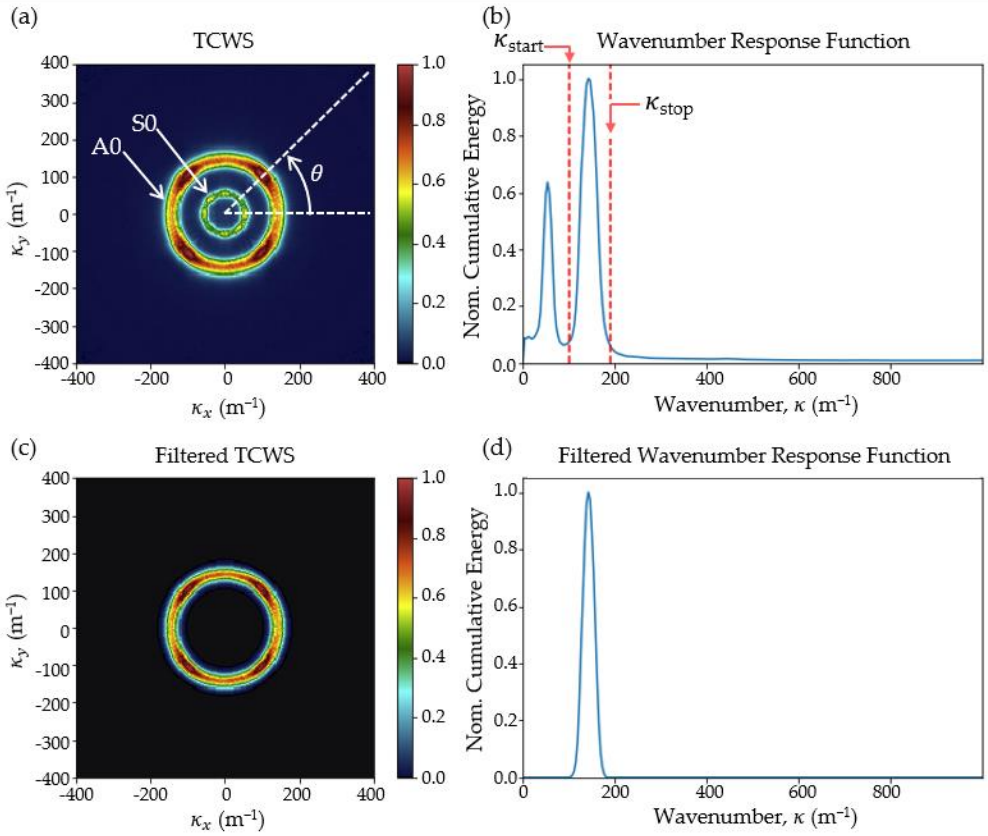

Figure 3. Example visualization of wavefield data in the form of (**a**) TCWS, (**b**) WRF, (**c**) filtered TCWS, and (**d**) filtered WRF.

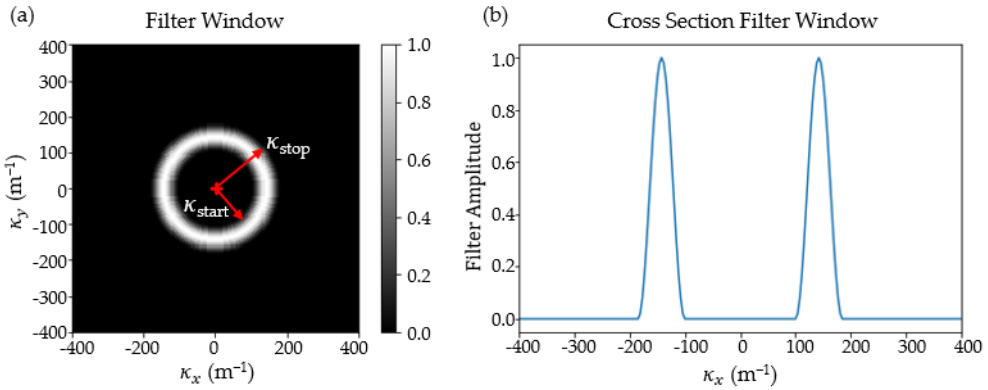

Figure 4. Example of a filter mask in its (**a**) top view and (**b**) cross-sectional view at $\kappa_y = 0$ m^{-1}.

2.2. Specimens and Flaws

Two specimens were prepared for experimental demonstration. Specimen A, which was a 500 by 500 by 2 mm^3 SUS304 stainless-steel plate, was used to validate the basic functionality of the proposed filter. The inspection was performed over a central 300 by 300 mm^2 region within which eight circular flaws, labeled (a) to (h) in Figure 5, were included. These flaws were created by milling away 1 mm of material on the inspection's reverse side, according to the diameters and central locations given in Table 1. Two corners of Specimen A were chamfered at 60 and 50 degrees. However, it is important to

note that these chamfers were part of a different study focused on non-orthogonal edge reflections and are not relevant to this paper; thus, their effects are not discussed here. The sensing point was located at the center of Specimen A's reverse side, indicated by the sensor-bonding location in Figure 5b.

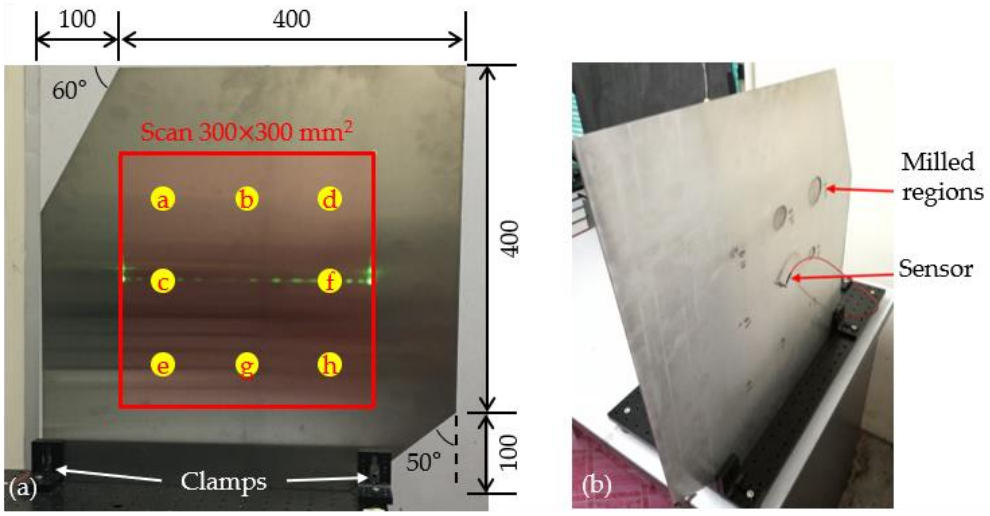

Figure 5. Specimen A: (**a**) Front view highlighting the scanning region and positional labels for hidden flaws. (**b**) Reverse side showing a centrally bonded sensor and multiple milled regions representing hidden flaws.

Table 1. Diameter and locations of flaws with reference to the bottom-left corner of the specimen.

Flaw Label	Diameter (mm)	Center x, y (mm)
a	40	150, 350
b	30	250, 350
c	20	150, 250
d	10	350, 350
e	5	150, 150
f	3	350, 250
g	2	250, 150
h	1	350, 150

Specimen B was prepared to demonstrate the enhanced flaw visibility afforded by the improved wavenumber resolution of the proposed filter. A subtle flaw was required for this demonstration; thus, a simple aluminum plate with six fasteners, where all except one were properly tightened, was used as the specimen. Specifically, the subtle flaw was simulated by adjusting the tightness level of one fastener away from its nominal tightness. It should be noted that the loosening of fasteners in aerospace structures is considered a significant structural flaw that can cause catastrophic accidents [41,42]. Also, prior attempts employing the GUPI system [43–46] have not achieved the necessary resolution to directly visualize partially tightened fasteners. Even when visualization is possible, a slightly tightened fastener would appear indistinguishable from those that are fully tightened in their results. In this study, the specimen was a 500 by 500 by 2 mm^3 plate made from aluminum alloy 6062. The inspection was confined to the central 260 by 260 mm^2 region. Within this region, six holes, each with a diameter of $\phi = 6.7 \pm 0.3$ mm, were polar symmetrically drilled 100 mm from the plate's center, through which stainless-steel M6 $\times$ 16 mm bolts and nuts were inserted, as depicted in Figure 6. The bolt heads were positioned on the inspection side, while the nuts were fastened on the reverse side of Specimen B. Bolts B1 to B5 were uniformly tightened to a nominal torque of 100 lb-in using a generic torque wrench. However, the target bolt, labeled TB, underwent partial tightening at various levels, commencing from 0 lb-in (hand tightened without using any tool) and incrementally

increasing by 20 lb-in up to 100 lb-in, following the inspection sequence outlined in Table 2. The sensing point was located at the center of Specimen B's reverse side, indicated by the sensor-bonding location in Figure 6b.

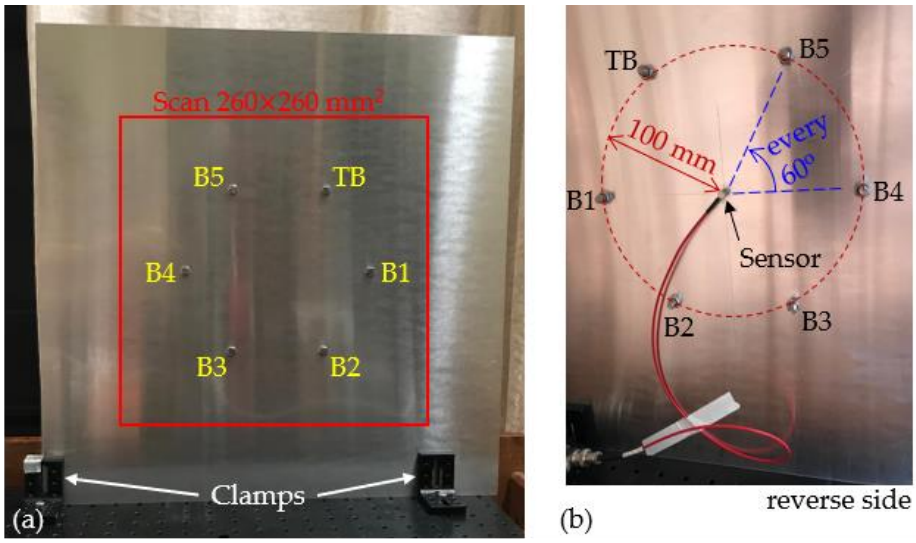

Figure 6. Specimen B: (**a**) Front view highlighting the scanning region and labels for bolts. (**b**) Reverse side showing a centrally bonded sensor and the relative positions of the bolts.

Table 2. Tightness level of target fastener in different inspections.

Inspection Sequence		1	2	3	4	5	6
Torque level	(lb-in)	0	20	40	60	80	100
	(Nm)	0.00	2.26	4.52	6.78	9.04	11.30

2.3. Data Acquisition

Guided ultrasonic wavefield data were obtained using a pulsed laser-scanning ultrasonic wavefield propagation imaging (UWPI) system, depicted in Figure 7. This system utilized a "scanning generation scheme" (SGS) [1] involving grid-points–scanning generation (actuation) and fixed-position sensing, resulting in wavefields visualized as emerging from the sensing position due to time reciprocity. Ultrasound was non-destructively generated using a diode-pumped solid-state Q-switched pulsed laser (Advanced Optowave Inc., Ronkonkoma, NY, USA), with the pulse energy set to approximately 1.5 mJ. The laser's characteristics included a wavelength of 532 nm, a beam diameter of about 4 mm, a pulse width of around 40 ns, and a pulse repetition frequency of 50 Hz. A galvanometric laser mirror scanner (ScanCube7, ScanLab GmbH, Puchheim, Germany) facilitated rectilinear grid-point scanning. The spatial sampling resolution was maintained at 0.5 mm in both horizontal x and vertical y directions. An amplifier-integrated PZT sensor (M304-A, Fuji Ceramics Corp., Fujinomiya, Japan), affixed to the reverse side of the specimens with cyanoacrylate adhesive, was used to measure the wavefield. Analog signals from the sensor were conditioned (amplified and filtered) using a variable cut-off frequency filter (3627, NF Corp., Yokohama, Japan) set to a suitable bandpass frequency, to be detailed later with the results. An 8-bit oscilloscope (USB-5133, National Instrument Corp., Austin, TX, USA) digitized each analog signal into 500 discrete samples. This actuation-measurement process was executed for all scanning grid points sequentially, culminating in the acquisition of 3D space–time wavefield data $v(x, y, t)$.

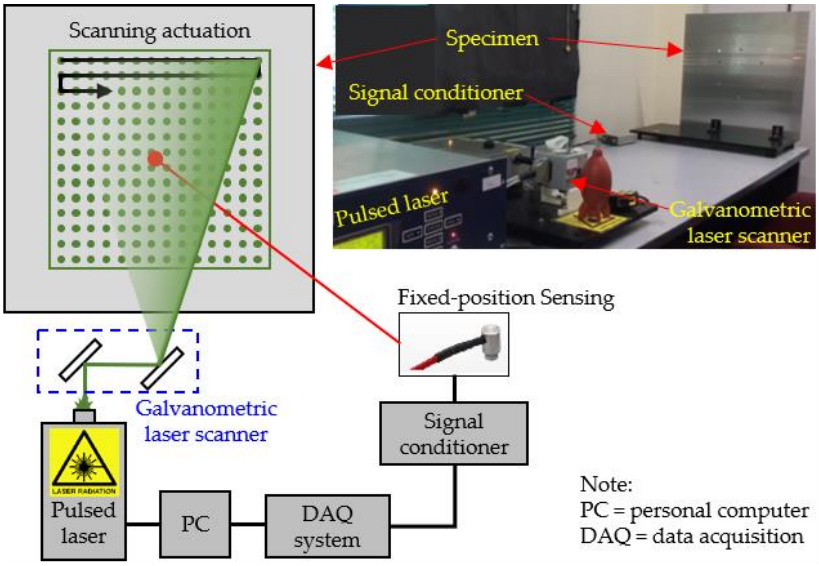

Figure 7. Schematic of UWPI system, with an inset of typical experimental setup.

3. Results

This section presents experimental results that substantiate the proposed wavenumber bandpass filter's capabilities. Section 3.1 employs theoretical dispersion curves for the identification of ultrasound modes within the specimen, aiding in contextualizing the selection of the wavenumber filtering band and validating the filter's functionality. Section 3.2 demonstrates the filter's effectiveness in amalgamating ultrasound features (target-specific energy or information) across a wider frequency range to enhance the visibility of hidden flaws. Lastly, Section 3.3 focuses on the filter's ability to detect and evaluate subtle flaws, underlining its potential for comprehensive and detailed inspections. Collectively, this section emphasizes the innovative aspects and impact of the proposed filter for NDT of aerospace structures and materials.

3.1. Validation of Filter Functionality

This subsection validates the basic functionality of the proposed wavenumber bandpass filter. Wavefield data measured from Specimen A after a narrow frequency bandpass filtering at f = 290~310 kHz was used. Prior to wavenumber filtering, these data can be visualized as wavefield freeze-frames at propagation instance t = 40 μs and t = 82 μs, as shown in Figure 8a,b, respectively. The wavefield can be observed emerging from the sensing position and propagating radially outward due to time reciprocity. Distinctive wavefield patterns, indicative of hidden flaws, emerge as wavefronts intersect the flaws' locations. The wavefield can also be transformed into a spectral energy map (SEM) [33,35] for single-image (instead of video) visualization, as displayed in Figure 8c. However, the SEM's high-energy central region, associated with the source, potentially obscures the hidden flaws. An attempt to enhance flaw visibility by re-generating the SEM after masking the central region followed by a self-normalization was, however, unsuccessful, as shown in Figure 8d, suggesting that interference of wavefield mode/wavenumber components in the specimen significantly affects flaw visibility. Nevertheless, to avoid overshadowing the source [47], masking the central region with a 100 mm diameter is continued as a default step during the preparation of other SEM images. More discussion on the masking of sources is available in Section 4.7.

The basic functionality of the proposed wavenumber bandpass filter is verified through its ability to separate mode/wavenumber components for interference-free visualization of the flaws. To comprehend the mode contents within Specimen A and accordingly tailor the selection of the wavenumber bandpass range, phase and group velocity dispersion data were generated using Vallen Dispersion software [48] and then converted into frequency–

wavenumber ($f - \kappa$) dispersion curves, as depicted in Figure 9a. This $f - \kappa$ plot delineates the two fundamental symmetrical and asymmetrical modes, i.e., the S0 and A0 modes, for the 2 mm thick stainless-steel Specimen A and its 1 mm thick flaw regions. At the central frequency of the bandpass (300 kHz), the S0 mode in both thickness regions exhibits a wavenumber range of approximately κ = 58.1~58.8 m^{-1}. In contrast, the A0 mode for the 2 mm thick, pristine regions is distinctly separated from that of the 1 mm thick flawed regions, exhibiting a wavenumber of κ = 153.4 m^{-1} for the pristine regions and κ = 200.1 m^{-1} for the flawed regions. With this understanding, the two prominent peaks and a small bump in the WRF, as shown in Figure 9b, can be, respectively, correlated with the S0 modes of both thicknesses, the A0 mode of the 2 mm thick pristine regions, and the A0 mode of the 1mm thick flawed regions. Performing wavenumber bandpass filtering for the data using a Hann window (α = 1.0) and the range of κ = 33~87 m^{-1} generated an SEM with a high-energy distribution throughout, as shown in Figure 10a, proving ineffective for flaw visualization due to the coexistence of S0 modes. Subsequent filtering at κ = 128~182 m^{-1} and then κ = 191~245 m^{-1} produced two SEMs highlighting the 2 mm thick pristine regions and the 1 mm thick flawed regions, respectively, as shown in Figure 10b,c. With the clear visualization of flaws of $\phi \geq 10$ mm and vague visualization of the flaw of $\phi = 5$ mm, as indicated in Figure 10c, the effectiveness of the proposed wavenumber bandpass filter is thereby affirmed. The visibility or detectability of smaller flaws is further discussed in Section 4.4.

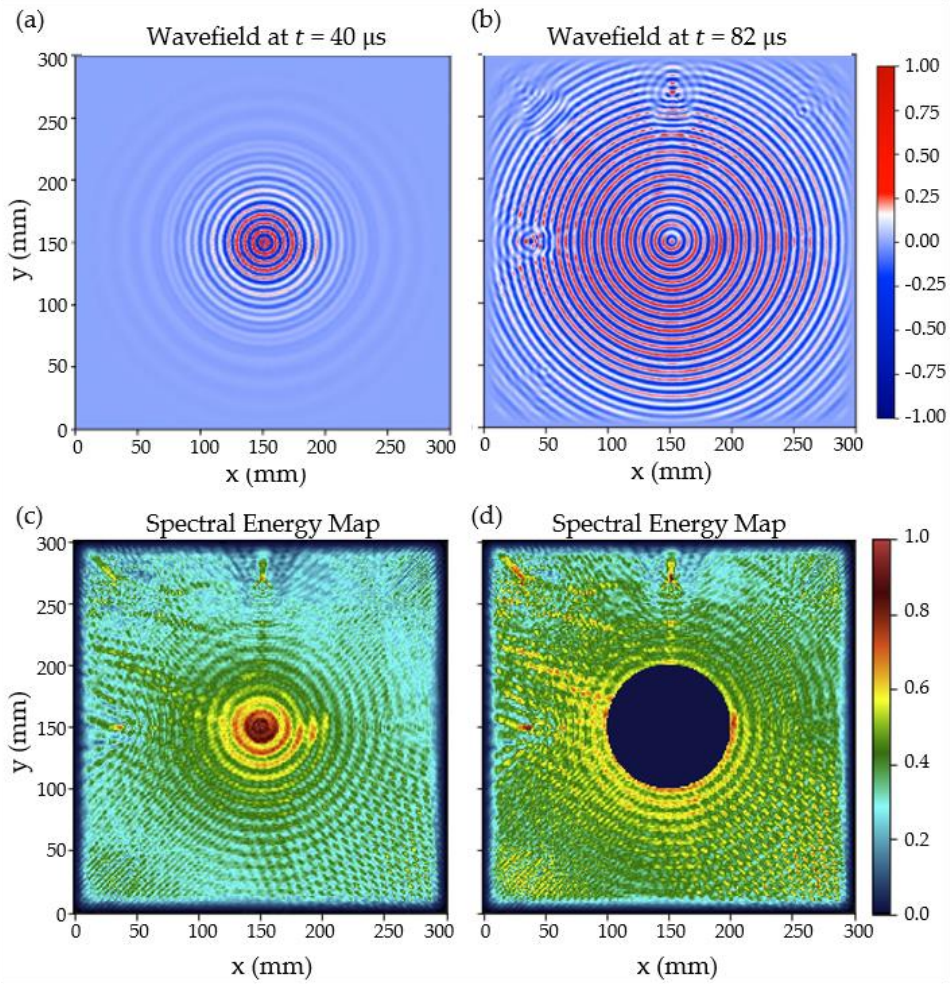

Figure 8. Wavefield of Specimen A before filtering, displayed as follows: (**a**) wavefield freeze-frame at 40 μs; (**b**) wavefield freeze-frame at 82 μs; (**c**) SEM; and (**d**) SEM with self-normalization after masking away the central region.

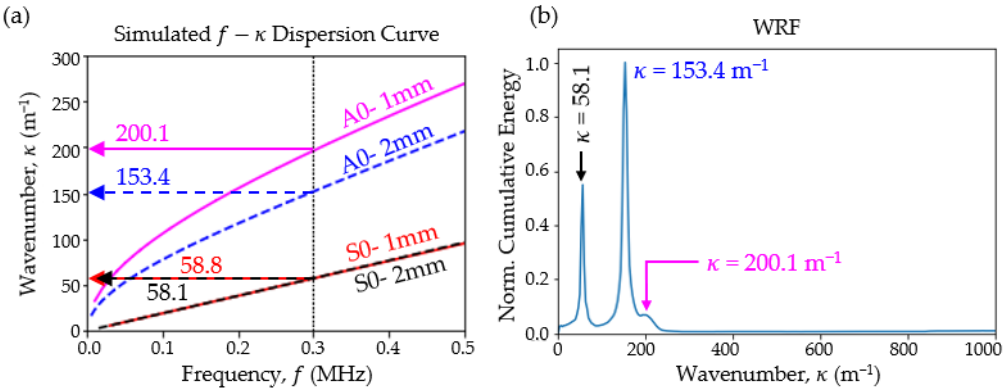

Figure 9. Identification of wave modes through (**a**) simulated $f-\kappa$ dispersion curves and (**b**) experimental WRF.

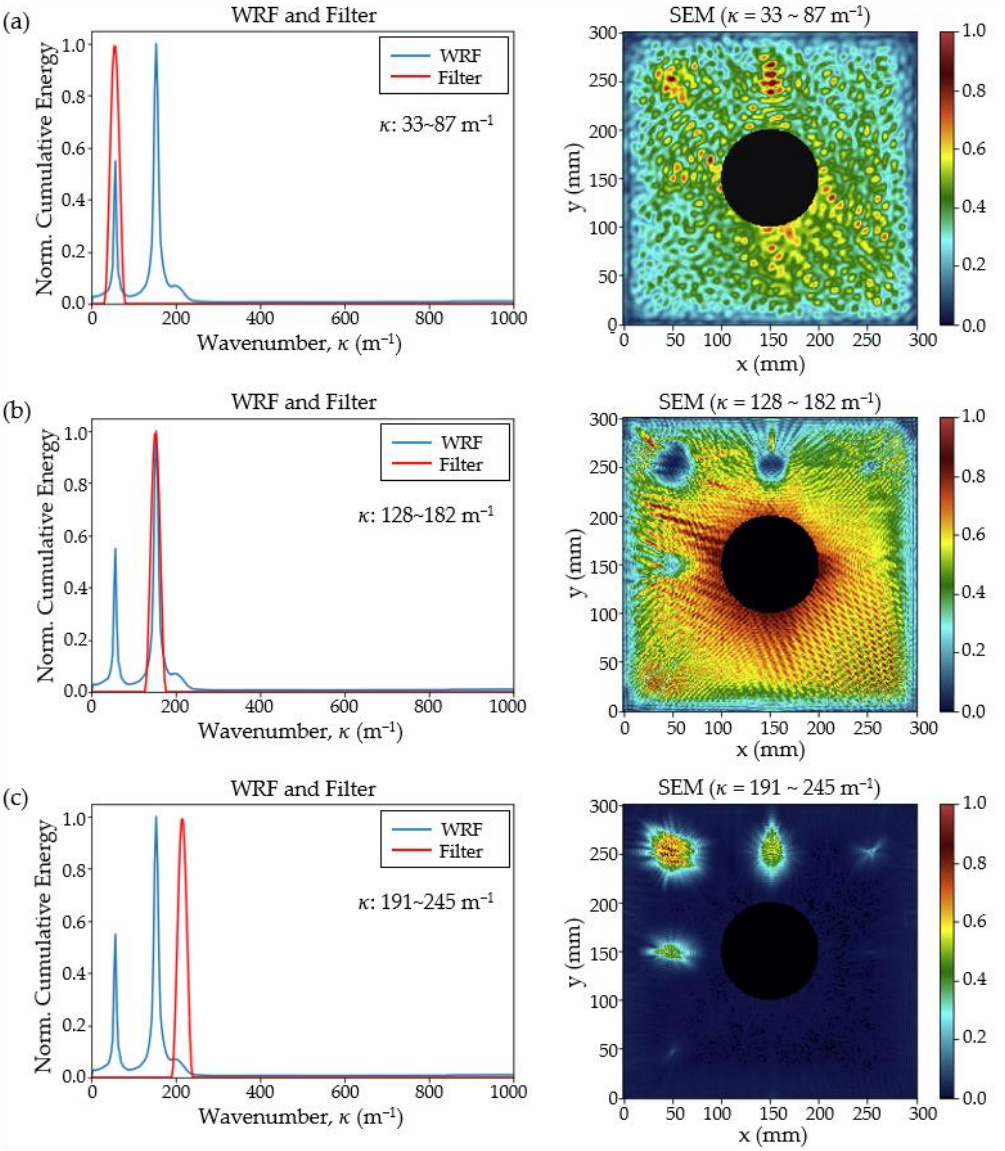

Figure 10. Filtering at different wavenumber bandpass ranges using a Hann window: (**a**) κ = 33~87 m^{-1}; (**b**) κ = 128~182 m^{-1}; (**c**) κ = 191~245 m^{-1}. The positive half of the filter cross-sectional view is overlaid on the WRF to indicate the effective filtering band.

3.2. Consolidation of Information across Frequencies

This subsection illustrates the proposed wavenumber bandpass filter's ability to consolidate valuable information across a broad frequency spectrum. The notion of improving imaging quality by fusing useful information from more than one set of data, each acquired using different measurement modalities or parametric settings, such as frequency, has been highlighted in a recent imaging roadmap [49]. Essentially, the proposed filter aggregates wavefield energy from all components within a selected wavenumber range, regardless of their frequency distribution. For this demonstration, wavefield data from Specimen A, filtered over a wide frequency band of f = 150~450 kHz, was utilized. The resulting WRF, presented in Figure 11a, no longer displays distinct, sharp peaks for the S0 and A0 modes. Instead, two major peaks, likely representing partially merged S0 and A0 modes, are identifiable. The small bump, previously associated with the A0 mode of the 1 mm thick flawed regions in Figure 9b, is now indiscernible in Figure 11a, possibly due to complete merging with adjacent modes. However, applying wavenumber bandpass filtering using a Hann window within the range of κ = 191~245 m^{-1} produced a SEM, as seen in Figure 11b, which exhibits enhanced flaw visibility compared to the earlier SEM in Figure 10c derived from narrower frequency bandwidth data. Notably, the $\phi = 5$ mm flaw is now distinctly visible, with smaller flaws of $\phi = 3$ mm and 2 mm vaguely detectable. This outcome emphatically validates that the proposed filter can effectively consolidate flaw-related information from a wide frequency range, even when individual modes are merged in the WRF and unidentifiable by comparison with dispersion curves. For comparison, Figure 11c shows the SEM of the data without wavenumber bandpass filtering. As an ancillary observation, the shape of the high-energy regions depicted in Figure 11b does not conform to the circular shape of the flaws. This discrepancy is most likely attributable to the acoustic lens effect, as discussed in references [50–52], which is beyond the scope of this study.

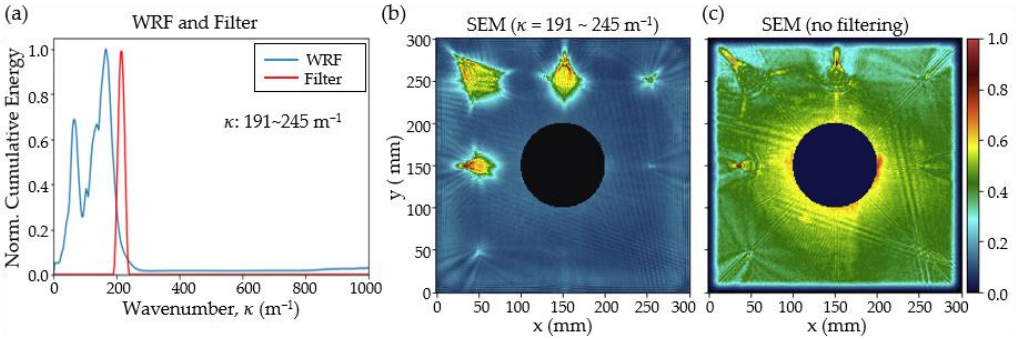

Figure 11. Consolidation of information across a wide frequency range using wavenumber bandpass range κ = 191~245 m^{-1}: (**a**) Relative position of the filter window overlaid on WRF. (**b**) SEM image after filtering and (**c**) without filtering, with a shared color bar.

3.3. Evaluation of Subtle Flaws

This subsection demonstrates the proposed filter's ability to selectively extract scarce flaws-relevant information for assessing subtle flaws, a capability made possible by its improved wavenumber resolution. To fully leverage the filter's capability for consolidating information across a wide frequency range, wavefield data were acquired from Specimen B over a broad frequency bandwidth of f = 20~1000 kHz. The S0 and A0 modes of the wavefield at 19 μs can be observed emerging from the sensing position and propagating radially outward in Figure 12a. Reflections from the fasteners are evident at a later propagation time of 25 μs, as depicted in Figure 12b. Notably, the reflection from the target bolt, which was left untightened at 0 lb-in during the data acquisition, is more pronounced than those from properly tightened bolts B1~B5. An initial study [40] has shown that vital loosening information is predominantly found within the wavenumber range κ = 40~90 m^{-1}. By filtering the data using a Tukey mask at α = 0.5 and a refined wavenum-

ber band κ = 38~111 m^{-1}, varied energy distributions around the bolts can be visualized through an SEM, as illustrated in Figure 12c. Further discussion on the window shape and size is given in Section 4.3. Note that the central region of 40 mm diameter was masked away to avoid overshadowing by the source. Significantly, the energy pattern around the target bolt is distinctly different from that surrounding the other bolts, highlighting the effective detection of a loosened fastener through SEM visualization facilitated by the proposed filter.

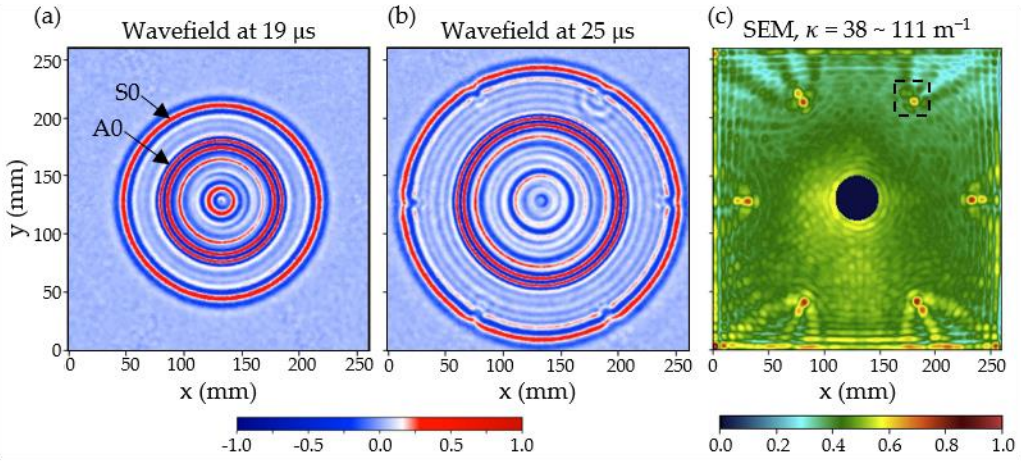

Figure 12. Inspection results of Specimen B when the target bolt was left untightened at 0 lb-in, given as wavefield freeze-frames at (**a**) 19 μs and (**b**) 25 μs, as well as (**c**) SEM after wavenumber bandpass filtering at κ = 38~111 m^{-1}.

To demonstrate the high wavenumber resolution of the proposed filter that enables direct visualization of partially loosened fasteners, the wavefield data from Specimen B, acquired while the target bolt was partially tightened according to Table 2, underwent filtering using the same wavenumber bandpass. The filtered data were then processed into SEMs for visualization. Figure 13, zooming in on the region outlined by the dashed box in Figure 12c encompassing the target bolt, displays the SEMs for varying bolt tightness conditions. The energy pattern of the untightened target bolt, as seen in Figure 13a, is markedly distinct from the other cases, characterized by a single primary energy 'blob'. As the bolt's tightness gradually increases, an adjacent secondary energy 'blob' starts to emerge. At 20 lb-in, the secondary 'blob' started to appear, as shown in Figure 13b. It progressively separates from the primary 'blob' at 40 lb-in, shown in Figure 13c, and attains full size by 60 lb-in, as depicted in Figure 13d. Instead of monotonous size enlargement with a further increment of bolt's tightness, the secondary 'blob' exhibited marginal amplitude increment along with slight size fluctuation at 80 lb-in and 100 lb-in. The chronology observable in these SEMs shows that the tightness level of a bolt can be visually distinguished using the GUPI system, which leverages the capabilities of the proposed wavenumber bandpass filter. Quantitative evaluations, like correlating ultrasound energy with bolt tightness levels, require extensive theoretical analysis beyond the scope and length of this paper and will be addressed in a separate, forthcoming publication.

Lastly, it is important to note that the differences in energy patterns observed between the 80 lb-in cases and the 100 lb-in cases in Figure 13e and 13f, respectively, are not as pronounced compared to those at lower bolt tightness levels. This phenomenon is consistent with the Contact Saturation Phenomenon reported by other research groups [53–55]. Although the wavenumber bandpass filter proposed in this work provides unprecedented high resolution compared to previous attempts employing the GUPI system [43–46], an even higher resolution is needed to achieve a more obvious difference in energy patterns at higher bolt tightness levels. The high sensitivity of nonlinear ultrasonic methods, such as those employing harmonics or resonance modes generation [56–58], could potentially be harnessed and incorporated into the GUPI processing in the future.

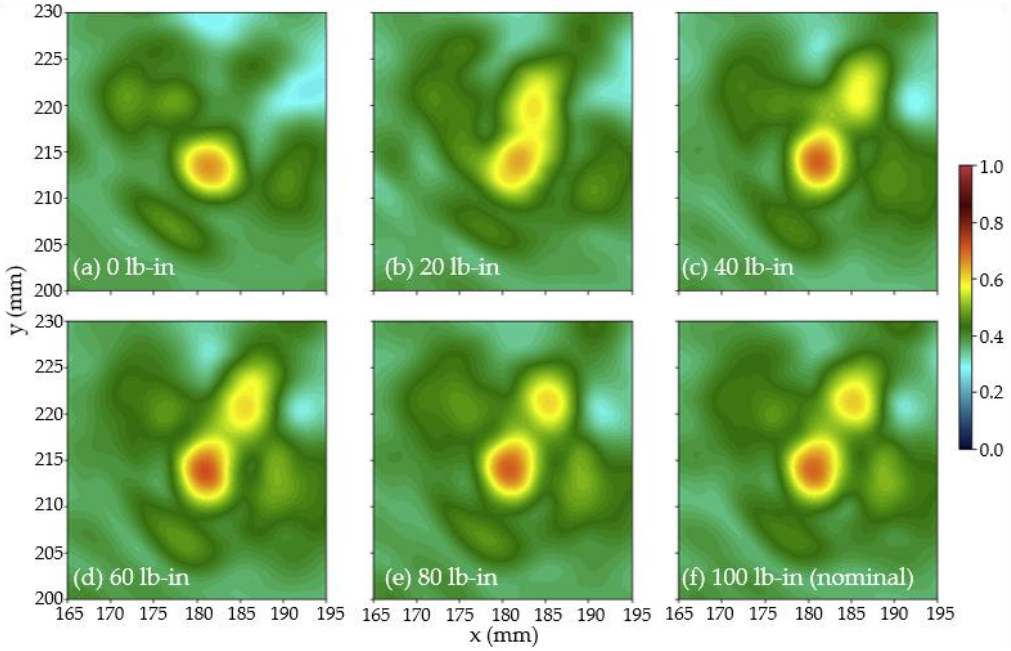

Figure 13. SEM at different bolt tightness levels zoomed in around the target bolt.

4. Discussion

This section offers a concise discussion of the results and their broader implications, delving into various facets of the proposed wavenumber bandpass filter. It begins with a comparison to the mode filter, highlighting the unique features and potential benefits of the proposed filter. The principles of flaw visibility, the suitability of different filter window shapes and sizes, and factors affecting flaw detectability are then examined. The applicability of the filter to structures made of different materials and methods for optimizing the wavenumber bandpass range when wavefield modes are not discernible through WRF or theoretical analysis are also discussed. Additionally, the necessity of masking the wavefield source and positioning the sensor equidistantly from all potential flaws is addressed. Throughout the section, suggestions for coping with situations different from those demonstrated in this paper are provided whenever specific challenges are identified.

4.1. Comparison with Mode Filter

The proposed wavenumber bandpass filter offers at least two distinct advantages over the mode filter [33]. First, unlike the mode filter, which is only applicable to narrow-frequency wavefield data with completely separated modes in the WRF for mode identification and subsequent wavenumber band determination, the wavenumber bandpass filter is not limited by the frequency bandwidth of the data. This flexibility allows it to consolidate useful information across a broader spectrum, enhancing flaw visibility. Section 3.2 and Section 3.3 demonstrate that this filter overturns the long-standing belief that modes must be separated based on narrow-band analysis to achieve high flaw visibility. Additionally, the mode filter's filtering limits are fixed, which significantly constrains its applicability in scenarios where the spectral information of interest is interspersed among other prominent spectral peaks in the WRF. In contrast, the proposed wavenumber bandpass filter can be applied to any wavenumber range of interest.

4.2. Principle of Flaw Visibility

The principle underlying the visibility of hidden flaws is closely related to the isolation of so-called "anomalous waves" [27,28]. Anomalous waves are generated through mode conversion when incident modes interact with structural flaws. These waves exhibit

slightly different frequency and wavenumber values compared to the incident modes. This difference is illustrated in the $f - \kappa$ plot presented in Figure 9a. In this figure, the magenta curve, representing the mode-converted A0 anomalous waves corresponding to the 1 mm thick flawed regions, is located above the blue dashed curve, which represents the incident A0 mode corresponding to the 2 mm thick pristine region. Specifically, at 300 kHz, the incident A0 mode has a wavenumber value of κ = 153.4 m^{-1}, while the mode-converted A0 mode has a higher wavenumber value of κ = 200.1 m^{-1}, as shown in Figure 9b. This difference is exploited by the proposed wavenumber bandpass filter to isolate the anomalous waves for flaw visualization. Applying the filter using a wavenumber band of κ = 191~245 m^{-1}, which corresponds to the anomalous waves, enhances the visibility of flaws, as demonstrated in Figures 10c and 11.

4.3. Window Shape and Size

The proposed wavenumber bandpass filter was designed with a window shape defined by Equation (1), which allows the adoption of a Tukey window by setting $0 < \alpha < 1$; a Hann window by setting $\alpha = 1$ or a boxcar window by setting $\alpha = 0$. Demonstration of filtering using a Hann window and a Tukey window at $\alpha = 0.5$ was given in Section 3, leaving the Boxcar window undemonstrated. While a boxcar window is notorious for causing significant spectral leakage during Fourier transformation, such leakage does not occur during inverse Fourier transformation; thus, a Hann, Tukey, or even Boxcar window can be adopted without any adverse effect. While there is no obvious advantage of using a window with reduced weightage near the starting and ending edges, the Boxcar window is recommended as the default choice. In fact, the Boxcar window can fully extract the ultrasound information or energy within the filter range, potentially increasing the visibility of subtle flaws. As a demonstration, wavefield data of Specimen B was reprocessed using a Boxcar window of the same band at κ = 38~111 m^{-1}. The result, given in Figure 14 using the same normalization as Figure 13, clearly shows an increased energy contrast around the target bolt compared to Figure 13.

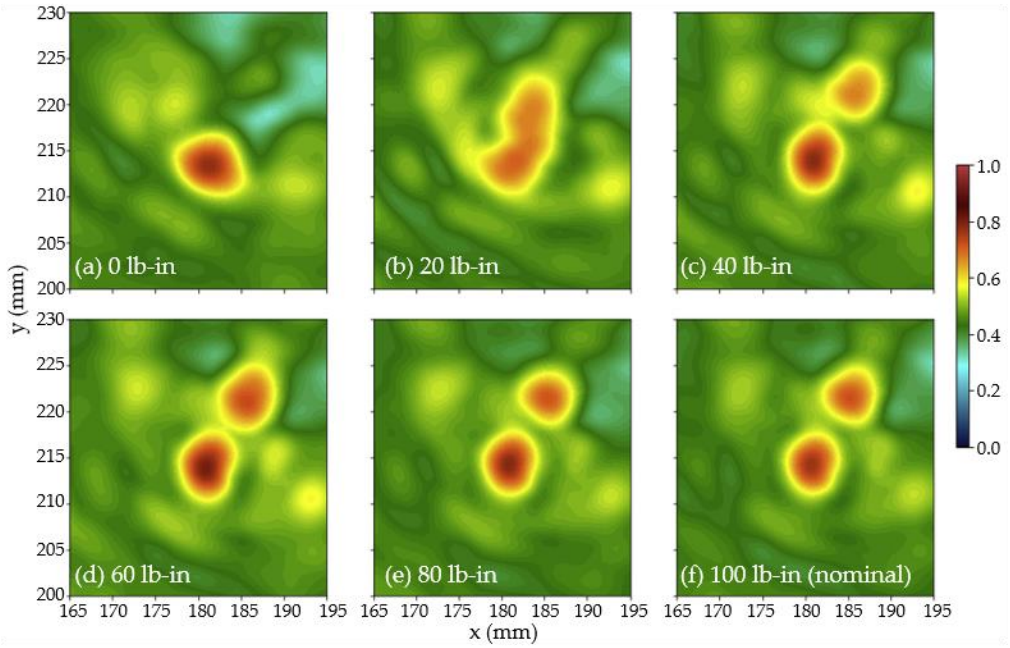

Figure 14. Increased energy contrast around the target bolt after filtering using a Boxcar window.

With regards to the filter window size, it is important to note that the wavefield data is discrete in the wavenumber domain due to discrete grid-point scanning during data acquisition, implying that the minimum settable window size is limited by the discretization resolution of the data. Discretization resolution for κ_x and κ_y is governed by the sampling

interval d and the number of sampling points n in respective spatial axes, as shown by the wavenumber bin centers generalized by Equation (7). It is apparent that a better wavenumber resolution can be achieved not by using a smaller interval d, but by increasing the size of the scanning region of interest, i.e., $(d \times n)$. Furthermore, although the proposed filter can set the arbitrary window size, limited only by the wavenumber discretization resolution, it is important to keep in mind that setting a very narrow window might leave insufficient discrete points to fully define the shape of the desired Tukey or Hann window. The boxcar window is anyhow unaffected by the window size.

$$bin\ centers = \begin{cases} \left[0,\ 1,\ \ldots,\ \frac{n}{2}-1, -\frac{n}{2},\ \ldots, -1\right] \ /\ (d \times n) & ;\ \text{if } n \text{ is even} \\ \left[0,\ 1,\ \ldots,\ \frac{n-1}{2}, -\frac{n-1}{2},\ \ldots -1\right] \ /\ (d \times n) & ;\ \text{if } n \text{ is odd} \end{cases} \quad (7)$$

4.4. Detectability of Flaws

The Nyquist–Shannon Sampling Theorem posits that a continuous signal can be accurately sampled and perfectly reconstructed from its samples if sampled at a rate at least twice the highest frequency present in the signal. Extending this theorem to GUPI spatial domain sampling implies that GUPI results support accurate detection of 1 mm flaws if the spatial sampling resolution (scan points interval) is 0.5 mm or less. However, as evidenced by results from Specimen A, this principle is not directly applicable to the GUPI system since the frequency content within a wavefield also significantly influences flaw detectability. For instance, before wavenumber bandpass filtering, most flaws in Figure 8d are undetectable, yet many become detectable with a broader frequency bandwidth in Figure 11c, albeit with poorly defined shapes.

Flaws detectability is directly affected by the wavelength (i.e., the reciprocal of wavenumber) contents of the wavefield. Previous empirical results [26] showed that the size of a flaw can be accurately measured when the wavelength is one-third or shorter than the minimum areal dimension of the flaw. This is more stringent than the theory, which requires the wavelength to be half or shorter than the flaw size. Nevertheless, the requirement is much more relaxed for qualitative flaw detectability or visibility. For instance, Figure 11b, which contained wavelength components λ = 4.08~5.24 mm due to wavenumber bandpass filtering at κ = 191~245 m^{-1}, shows the flaws of $\phi \geq 5$ mm clearly and other smaller flaws ($\phi = 3$ mm and 2 mm) vaguely, even though only flaws of $\phi \geq 8.16$ mm can be accurately measured as the theory would suggest. Anyhow, despite the criticality of quantitative flaw size measurement in NDT applications, it is beyond the scope of this paper to further discuss the accuracy of size measurement.

The detection and clear visualization of the real flaws could be more challenging compared to the artificial flaws used in this study. Several factors may contribute to this difficulty. For instance, real structural thinning due to erosion may exhibit a progressive change in thickness across different spatial locations rather than the step change shown by the artificial flaws in Specimen A. With a subtler variation in flaw severity, the wavenumber of mode-converted anomalous waves may deviate less from that of incident modes, necessitating a higher wavenumber resolution in the filter for effective flaw visualization.

4.5. Optimization of Wavenumber Bandpass Range

The typical process of determining the most effective wavenumber bandpass ranges for visualizing flaws involves examining the WRF against the $f - \kappa$ dispersion curves of a specimen, as demonstrated for Specimen A in Figure 9. However, this approach faces limitations under certain conditions. First, the theoretical dispersion curves of the specimen might not be available due to the unknown material properties, which could stem from proprietary issues or military secrecy. Second, when the wavefield data covers a broad frequency range, the peaks for different modes may be partially or fully merged, as shown in Figure 11a, hindering the identification of distinctive modes necessary for band analysis. Third, geometrically complex structures, such as those with varying local thicknesses or those constructed from multiple materials, tend to have a complex wavenumber spectrum

that does not facilitate straightforward band optimization. In such cases, without specific insights into the mode contents, selecting an optimal wavenumber bandpass range for flaw visualization is like a blind guess. Fortunately, conducting an extensive search within the wavenumber domain for various bandpass ranges is feasible. This is due to the efficient processing of 2D Discrete Fourier Transform (DFT) and inverse DFT (iDFT) relative to the 3D counterparts and the possibility of performing DFT just once during the bandpass search (recursive iDFT is still needed). When an extensive search is needed, the typical filter process shown in Figure 1 can be repeated by programmatically setting different κ_{start} and κ_{stop} value combinations over the desired wavenumber searching range. Performing wavenumber filtering and displaying the result as an SEM can be accomplished swiftly using a standard personal computer or laptop. To provide a rough idea for the processing time, an SEM for Specimen A can be produced in under 20 s using a computer (3.2 GHz 12th generation Intel® Core™ i9-12900K, 64 GB RAM, 64-bit Windows 10 Pro) without any specialized hardware accelerators or parallel processing.

4.6. Suitability for Different Materials

It is expected that the proposed wavenumber bandpass filter can be applied to thin-walled structures made of different isotropic materials. Ultrasound waves propagate in different materials at different speeds, and these differences can be visualized through the $f - \kappa$ dispersion curves. The $f - \kappa$ dispersion curves for generic 1 mm thick aluminum, steel, and titanium plates for frequencies up to 0.5 MHz are shown in Figure 15. Three curves represent the S0 mode near the lower part of the figure, and another three curves represent the A0 mode above them. Figure 15 clearly shows a minor slope difference for different isotropic materials while maintaining a similar overall pattern. It is further expected that the experimental WRFs of different materials would follow a generally similar pattern to the one shown in Figure 9b, with minor differences in mode peak positions. Therefore, it is strongly believed that the proposed wavenumber bandpass filter is applicable for wavefields measured from thin-walled structures made of different isotropic materials, perhaps with a minor adjustment to the wavenumber bandpass range corresponding to the features of interest to be isolated. Suitability for anisotropic materials requires further investigation. Based on current understanding, anisotropic materials might have non-circular wavefronts and TCWS, causing errors during the generation of WRF through polar consolidation of TCWS. Ultimately, these errors might result in the over-spreading of information from a specific wavenumber bin to neighboring wavenumber bins, reducing the accuracy of the proposed filter.

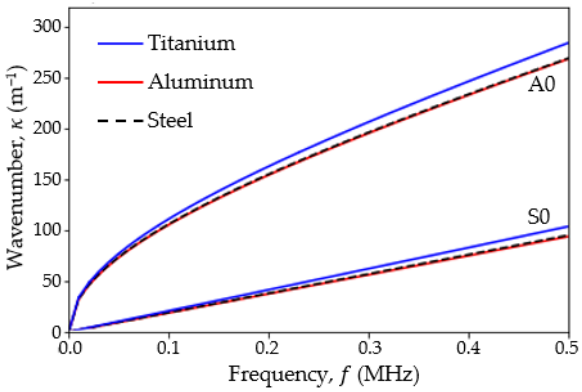

Figure 15. Simulated $f - \kappa$ dispersion curves for 1 mm thick aluminum, steel, and titanium plates.

4.7. Masking of Wavefield Source

As stated in Section 3.1, the high-energy central region of almost all SEMs presented in this paper was masked to avoid the overshadowing effect of the wavefield source [47]. This source masking was a preference rather than a necessity aimed at enhancing the visibility of hidden flaws. Specifically, ultrasound energy is significantly higher at the source point and

rapidly decreases with increasing distance from the source due to energy spreading and attenuation [59]. When the source is located within an imaging region, a large portion of the available image contrast is used to display the significantly higher energy region around the source, reducing the available contrast for other purposes, such as flaw visualization. As a result, a bright spot appears around the source, but the flawed region may have a similar intensity to other non-flawed regions, making flaw visualization more difficult. This overshadowing effect has been recognized previously, and masking a region around the source point was proposed [47] and adopted in this work. However, source masking poses a high risk of missing potential flaws located within the masking radius. Therefore, it must be used with great care and is only recommended when the existence and exact positions of all flaws in a specimen are known. If this condition is not met, the overshadowing effect should be reduced using alternative methods, such as the weighted root mean square methods [11,32].

4.8. Source Positioning

In this work, all wavefield measurements were conducted with the sensor placed at the center of the specimens. Due to elastodynamic reciprocity [60], the wavefield is perceived as emerging from the sensing (source) point. This central positioning is common in laboratory investigations when amplitude-normalized or energy-normalized signals are needed for meaningful comparison across multiple flaws without requiring signal processing-based normalization [29]. Specifically, wavefield spreading loss and attenuation [59] are functions of wavefield propagation distance. By ensuring the same displacement between the source and all flaws, uniform spreading loss and attenuation are maintained, eliminating the need for additional amplitude or energy normalization. In real-world scenarios, the positions of flaws are typically unknown a priori, making it impossible to benefit from normalization based on source positioning. Even when the positions of all potential flaws are known, such as when detecting the loosening of a row of fasteners [44,45], it is often impractical to position the source equidistantly from all potential flaws. In such cases, normalization using signal processing methods, such as the weighted root mean square method [11,32], is inevitable.

5. Conclusions

Guided ultrasonic wavefield propagation imaging (GUPI) is useful for visualizing hidden flaws in aerospace thin-walled structures. However, its wider acceptance is hindered by the challenge of extracting flaw-relevant information from its complex multimodal wavefield data. This difficulty primarily arises from one or a combination of the following problems: (i) subjective and/or complex customizations of processing steps; (ii) inefficient processing due to the 3D transformation from the space–time domain to the wavenumber–frequency domain and back; (iii) insufficient resolution to distinguish between flaw-relevant and flaw-irrelevant information in the wavefield data.

A wavenumber bandpass filter is proposed in this paper to address the difficulty. Beyond mitigating the aforementioned problems, the filter exhibits a unique capability of consolidating scarce flaw-relevant information within a specific wavenumber band from a wide frequency spectrum for enhanced visualization of subtle structural flaws. It also overturns the long-standing belief that modes must be separated based on narrow-band data acquisition or processing to achieve high flaw visibility. Its characteristics and advantages were described and experimentally demonstrated. Firstly, its efficacy was demonstrated by filtering thickness-specific information from the wavefield of a stainless-steel plate with multiple wall-thinned flaws, aligning with the thickness predictions of theoretical $f - \kappa$ dispersion curves. Furthermore, its unique capability to consolidate information was showcased through the visualization of these wall-thinned flaws with enhanced contrast and higher detectability for smaller flaws. Lastly, a demonstration of harnessing its advantages for direct visualization of subtle flaws through an unprecedented GUPI visualization of a partially loosened fastener in an aluminum plate was given. The

results clearly proved that the proposed wavenumber bandpass filter can effectively provide high-resolution filtering under a structured processing framework, i.e., without subjective ad hoc customizations.

Despite the aforementioned advantages, the proposed filter and the experimental work presented herein exhibit several limitations. Firstly, the wavenumber resolution needs to be further improved to detect and visualize subtler flaws, such as variations in bolt tightness of less than 20% from the nominal level. Additionally, all experiments conducted in this study were based on artificial flaws. It is necessary to perform analyses using more realistic specimens and flaws, such as evaluating real corrosion damage, detecting fastener loosening in lap-jointed specimens, and identifying non-areal flaws such as fatigue cracks. More quantitative evaluation should also be provided to facilitate a fair comparison with other research. Lastly, the proposed filter, in its current form, is not suitable for anisotropic structures, such as orthotropic fiber-reinforced composite materials. The filter requires refinement to better accommodate anisotropic materials, reflecting the prevalent use of fiber-reinforced composites in aerospace structures.

Aside from these limitations, several potential expansions have been identified. Firstly, the proposed filter has significant potential to improve wavenumber mapping [24,37] in terms of efficiency by substituting the 3D Fourier transformation with a 2D variant and in terms of clarity through information consolidation from a broader frequency spectrum. Its superior resolution in the wavenumber domain could help separate closely spaced modes in a wavefield, thus broadening the applicability of GUPI to thicker specimens and opening a gateway for scientific explorations of high-frequency wavefields. Isolating the wavefield modes of 1mm thick flawed regions in Specimen A exemplifies a basic mode-conversion analysis, which could be extended to more intricate and realistic scenarios in future research.

Author Contributions: Conceptualization, C.C.C.; methodology, C.C.C.; software, L.S.Y. and C.C.C.; validation, M.Y.H.; formal analysis, L.S.Y. and C.C.C.; investigation, L.S.Y.; resources, J.-R.L. and M.Y.H.; data curation, L.S.Y. and C.C.C.; writing—original draft preparation, L.S.Y.; writing—review and editing, C.C.C., M.Y.H., F.I.R., N.M. and J.-R.L.; visualization, L.S.Y.; supervision, M.Y.H., J.-R.L., N.M. and F.I.R.; project administration, M.Y.H.; funding acquisition, M.Y.H. All authors have read and agreed to the published version of the manuscript.

Funding: This research was funded by the Industrial Research Grant Scheme through the Endowment of Tan Sri Syed Azman Syed Ibrahim (Account Vote Number: 6338201-10801).

Data Availability Statement: The data presented in this study are available on reasonable request from the corresponding authors.

Acknowledgments: The authors acknowledge the support from Universiti Putra Malaysia and the Industrial Research Grant Scheme through Endowment Tan Sri Syed Azman Syed Ibrahim (Account Vote Number: 6338201-10801). The authors also acknowledge the support by the Defense Acquisition Program Administration and the Agency for Defense Development of the Republic of Korea under grant no. 99-402-805-032 (The integration of wireless sensing into aerial vehicles for structural damage identification).

Conflicts of Interest: The authors declare no conflicts of interest.

References

1. Chia, C.C.; Lee, S.Y.; Harmin, M.Y.; Choi, Y.; Lee, J.-R. Guided Ultrasonic Waves Propagation Imaging: A Review. *Meas. Sci. Technol.* **2023**, *34*, 052001. [CrossRef]
2. Zheng, S.; Luo, Y.; Xu, C.; Xu, G. A Review of Laser Ultrasonic Lamb Wave Damage Detection Methods for Thin-Walled Structures. *Sensors* **2023**, *23*, 3183. [CrossRef] [PubMed]
3. Chia, C.C.; Jang, S.-G.; Lee, J.-R.; Yoon, D.-J. Structural Damage Identification Based on Laser Ultrasonic Propagation Imaging Technology. In *Optical Measurement Systems for Industrial Inspection VI*; International Society for Optics and Photonics: Bellingham, WA, USA, 2009; Volume 7389, p. 73891S.
4. Viktorov, I.A. *Rayleigh and Lamb Waves: Physical Theory and Applications*; Ultrasonic Technology; Plenum Press: New York, NY, USA, 1967; ISBN 978-0-306-30286-2.

5. Rose, J.L. *Ultrasonic Guided Waves in Solid Media*; Cambridge University Press: Cambridge, UK, 2014; ISBN 978-1-107-04895-9.
6. Dawood, S.D.S.; Harithuddin, A.S.M.; Harmin, M.Y. Modal Analysis of Conceptual Microsatellite Design Employing Perforated Structural Components for Mass Reduction. *Aerospace* **2022**, *9*, 23. [CrossRef]
7. Dong, Z.; Wang, Z.; Tian, J.; Kang, R.; Bao, Y. Investigation on Tearing Damage of CFRP Circular Cell Honeycomb in End-Face Grinding. *Compos. Struct.* **2023**, *325*, 117616. [CrossRef]
8. Lyu, Y.; Niu, Y.; He, T.; Shu, L.; Zhuravkov, M.; Zhou, S. An Efficient Method for the Inverse Design of Thin-Wall Stiffened Structure Based on the Machine Learning Technique. *Aerospace* **2023**, *10*, 761. [CrossRef]
9. Dawood, S.D.S.; Harmin, M.Y.; Harithuddin, A.S.M.; Chia, C.C.; Rafie, A.S.M. Computational Study of Mass Reduction of a Conceptual Microsatellite Structural Subassembly Utilizing Metal Perforations. *J. Aeronaut. Astronaut. Aviat.* **2021**, *53*, 57–66. [CrossRef]
10. Chan, Y.N.; Harmin, M.Y.; Othman, M.S. Parametric Study of Varying Ribs Orientation and Sweep Angle of Un-Tapered Wing Box Model. *Int. J. Eng. Technol.* **2018**, *7*, 155–159. [CrossRef]
11. Rucka, M.; Wojtczak, E.; Lachowicz, J. Damage Imaging in Lamb Wave-Based Inspection of Adhesive Joints. *Appl. Sci.* **2018**, *8*, 522. [CrossRef]
12. Wang, J.; Shen, Y. An Enhanced Lamb Wave Virtual Time Reversal Technique for Damage Detection with Transducer Transfer Function Compensation. *Smart Mater. Struct.* **2019**, *28*, 085017. [CrossRef]
13. Wang, X.; Cai, J.; Zhou, Z. A Lamb Wave Signal Reconstruction Method for High-Resolution Damage Imaging. *Chin. J. Aeronaut.* **2019**, *32*, 1087–1099. [CrossRef]
14. Kang, T.; Yoon, M.; Han, S.; Kim, K.-M.; Koo, B. Selection of Optimal Exciting Frequency and Lamb Wave Mode for Detecting Wall-Thinning in Plates Using Scanning Laser Doppler Vibrometer. *Measurement* **2022**, *200*, 111676. [CrossRef]
15. Chen, H.; Ling, F.; Zhu, W.; Sun, D.; Liu, X.; Li, Y.; Li, D.; Xu, K.; Liu, Z.; Ta, D. Waveform Inversion for Wavenumber Extraction and Waveguide Characterization Using Ultrasonic Lamb Waves. *Measurement* **2023**, *207*, 112360. [CrossRef]
16. Kang, T.; Han, S.-J.; Han, S.; Kim, K.-M.; Kim, D.-J. Detection of Shallow Wall-Thinning of Pipes Using a Flexible Interdigital Transducer-Based Scanning Laser Doppler Vibrometer. *Struct. Health Monit.* **2022**, *21*, 2688–2699. [CrossRef]
17. Xia, R.; Wang, W.; Shao, S.; Wu, Z.; Chen, J.; Zhang, X.; Li, Z. Mode Purification for Multimode Lamb Waves by Shunted Piezoelectric Unimorph Array. *Appl. Phys. Lett.* **2023**, *122*, 201703. [CrossRef]
18. Huke, P.; Schröder, M.; Hellmers, S.; Kalms, M.; Bergmann, R.B. Efficient Laser Generation of Lamb Waves. *Opt. Lett.* **2014**, *39*, 5795–5797. [CrossRef]
19. Rothe, S.; Daferner, P.; Heide, S.; Krause, D.; Schmieder, F.; Koukourakis, N.; Czarske, J.W. Benchmarking Analysis of Computer Generated Holograms for Complex Wavefront Shaping Using Pixelated Phase Modulators. *Opt. Express* **2021**, *29*, 37602–37616. [CrossRef] [PubMed]
20. Kim, T.; Chang, W.-Y.; Kim, H.; Jiang, X. Narrow Band Photoacoustic Lamb Wave Generation for Nondestructive Testing Using Candle Soot Nanoparticle Patches. *Appl. Phys. Lett.* **2019**, *115*, 102902. [CrossRef]
21. Liu, Z.; Shan, S.-B.; Dong, H.-W.; Cheng, L. Topologically Customized and Surface-Mounted Meta-Devices for Lamb Wave Manipulation. *Smart Mater. Struct.* **2022**, *31*, 065001. [CrossRef]
22. Jeon, J.Y.; Kim, D.; Park, G.; Flynn, E.; Kang, T.; Han, S. 2D-Wavelet Wavenumber Filtering for Structural Damage Detection Using Full Steady-State Wavefield Laser Scanning. *NDT E Int.* **2020**, *116*, 102343. [CrossRef]
23. Michaels, T.E.; Michaels, J.E.; Ruzzene, M. Frequency–Wavenumber Domain Analysis of Guided Wavefields. *Ultrasonics* **2011**, *51*, 452–466. [CrossRef]
24. Flynn, E.B.; Chong, S.Y.; Jarmer, G.J.; Lee, J.-R. Structural Imaging through Local Wavenumber Estimation of Guided Waves. *NDT E Int.* **2013**, *59*, 1–10. [CrossRef]
25. Chia, C.C.; Gan, C.S.; Gomes, C.; Mazlan, N.; Gomes, A. Lightning Damages in Glass Fiber-Epoxy Composite Material Used for Aerospace Applications. In Proceedings of the 2018 34th International Conference on Lightning Protection (ICLP), Rzeszow, Poland, 2–7 September 2018; pp. 1–4.
26. Moon, S.; Kang, T.; Han, S.-W.; Jeon, J.-Y.; Park, G. Optimization of Excitation Frequency and Guided Wave Mode in Acoustic Wavenumber Spectroscopy for Shallow Wall-Thinning Defect Detection. *J. Mech. Sci. Technol.* **2018**, *32*, 5213–5221. [CrossRef]
27. Gan, C.S.; Chia, C.C.; Tan, L.Y.; Mazlan, N.; Harley, J.B. Statistical Evaluation of Damage Size Based on Amplitude Mapping of Damage-Induced Ultrasonic Wavefield. *IOP Conf. Ser. Mater. Sci. Eng.* **2018**, *405*, 012006. [CrossRef]
28. Gan, C.S.; Tan, L.Y.; Chia, C.C.; Mustapha, F.; Lee, J.-R. Nondestructive Detection of Incipient Thermal Damage in Glass Fiber Reinforced Epoxy Composite Using the Ultrasonic Propagation Imaging. *Funct. Compos. Struct.* **2019**, *1*, 025006. [CrossRef]
29. Segers, J.; Hedayatrasa, S.; Poelman, G.; Van Paepegem, W.; Kersemans, M. Self-Reference Broadband Local Wavenumber Estimation (SRB-LWE) for Defect Assessment in Composites. *Mech. Syst. Signal Proc.* **2022**, *163*, 108142. [CrossRef]
30. Zhang, H.; Sun, J.; Rui, X.; Liu, S. Delamination Damage Imaging Method of CFRP Composite Laminate Plates Based on the Sensitive Guided Wave Mode. *Compos. Struct.* **2023**, *306*, 116571. [CrossRef]
31. Harley, J.B.; Moura, J.M.F. Scale Transform Signal Processing for Optimal Ultrasonic Temperature Compensation. *IEEE Trans. Ultrason. Ferroelectr. Freq. Control.* **2012**, *59*, 2226–2236. [CrossRef] [PubMed]

32. Kudela, P.; Radzieński, M.; Ostachowicz, W. Identification of Cracks in Thin-Walled Structures by Means of Wavenumber Filtering. *Mech. Syst. Signal Proc.* **2015**, *50–51*, 456–466. [CrossRef]
33. Shahrim, M.A.A.; Chia, C.C.; Ramli, H.R.; Harmin, M.Y.; Lee, J.-R. Adaptive Mode Filter for Lamb Wavefield in the Wavenumber-Time Domain Based on Wavenumber Response Function. *Aerospace* **2023**, *10*, 347. [CrossRef]
34. Shahrim, M.A.; Harmin, M.Y.; Romli, F.I.; Chia, C.C.; Lee, J.-R. Damage Visualization based on Frequency Shift of Single-Mode Ultrasound-Guided Wavefield. *J. Aeronaut. Astronaut. Aviat.* **2022**, *54*, 297–305. [CrossRef]
35. Shahrim, M.A.A.; Lee, S.Y.; Lee, J.-R.; Harmin, M.Y.; Chia, C.C. Visualization of Water Ingress in Aluminium Honeycomb Sandwich Panel through Mode Isolation of Lamb Wavefield. *J. Aerosp. Soc. Malays.* **2023**, *1*, 9–18.
36. Basiri, E.; Hasanzadeh, R.P.; Kersemans, M. A Successive Wavenumber Filtering Approach for Defect Detection in CFRP Using Wavefield Scanning. In Proceedings of the 7th International Conference on Signal Processing and Intelligent Systems (ICSPIS), Tehran, Iran, 29 December 2021; pp. 1–6.
37. Spytek, J.; Dziedziech, K.; Pieczonka, L. Improving Efficiency of Local Wavenumber Estimation for Damage Detection in Thin-Walled Structures. *Mech. Syst. Signal Proc.* **2023**, *199*, 110470. [CrossRef]
38. Bae, D.-Y.; Lee, J.-R. Development of Single Channeled Serial-Connected Piezoelectric Sensor Array and Damage Visualization Based on Multi-Source Wave Propagation Imaging. *J. Intell. Mater. Syst. Struct.* **2015**, *27*, 1861–1870. [CrossRef]
39. Bae, D.-Y.; Lee, J.-R. A Health Management Technology for Multisite Cracks in an In-Service Aircraft Fuselage Based on Multi-Time-Frame Laser Ultrasonic Energy Mapping and Serially Connected PZTs. *Aerosp. Sci. Technol.* **2016**, *54*, 114–121. [CrossRef]
40. Lee, S.Y.; Chia, C.C.; Romli, F.I.; Mazlan, N.; Lee, J.-R.; Harmin, M.Y. Visualizing Partially Loosened Fastener through Frequency-Wavenumber Analysis of Ultrasonic Wavefield. *J. Aeronaut. Astronaut. Aviat.* **2024**, *56*, 147–155. [CrossRef]
41. ATSB. *Loss of Control—Robinson Helicopter R44 Astro VH-HFH, Cessnock Aerodrome, NSW, on 4 February 2011 (Report Number: AO-2011-016 Final)*; ATSB Transport Safety Report; The Australia Transport Safety Bureau: Canberra, ACT, Australia, 2012; p. 48.
42. NTSB. *Loss of Pitch Control on Takeoff Emery Worldwide Airlines, Flight 17 McDonnell Douglas DC-8-71F, N8079U Rancho Cordova, California February 16, 2000 (Report Number NTSB/AAR-03/02*; PB2003-910402; Notation 7299A); Aircraft Accident Report; The USA National Transportation Safety Board: Washington, DC, USA, 2003; p. 124.
43. Haynes, C.; Yeager, M.; Todd, M.; Lee, J.-R. Monitoring Bolt Torque Levels through Signal Processing of Full-Field Ultrasonic Data. In *Health Monitoring of Structural and Biological Systems, SPIE 9064*; SPIE: San Diego, CA, USA, 2014; Volume 9064, pp. 906428-1–906428-29.
44. Gooda Sahib, M.I.; Leong, S.J.; Chia, C.C.; Mustapha, F. Detection of Fastener Loosening in Simple Lap Joint Based on Ultrasonic Wavefield Imaging. *IOP Conf. Ser. Mater. Sci. Eng.* **2017**, *270*, 012035. [CrossRef]
45. Tola, K.D.; Lee, C.; Park, J.; Kim, J.-W.; Park, S. Bolt Looseness Detection Based on Ultrasonic Wavefield Energy Analysis Using an Nd:YAG Pulsed Laser Scanning System. *Struct. Control. Health Monit.* **2020**, *27*, e2590. [CrossRef]
46. Zhou, Y.; Yuan, C.; Sun, X.; Yang, Y.; Wang, C.; Li, D. Monitoring the Looseness of a Bolt through Laser Ultrasonic. *Smart Mater. Struct.* **2020**, *29*, 115022. [CrossRef]
47. Abbas, S.H.; Truong, T.C.; Lee, J.-R. FPGA-Based Ultrasonic Energy Mapping with Source Removal Method for Damage Visualization in Composite Structures. *Adv. Compos. Mater.* **2017**, *26*, 3–13. [CrossRef]
48. Vallen Systeme GmbH. *Vallen Dispersion*; Version R2008.0915; Vallen Systeme GmbH: Icking, Germany, 2008.
49. Lee, J.-R.; Yoo, H.; Chia, C.C.; et al. Roadmap on Industrial Imaging Techniques. *Meas. Sci. Technol.* 2024; *in press*.
50. Tian, Z.; Yu, L. Wavefront Modulation and Controlling for Lamb Waves Using Surface Bonded Slice Lenses. *J. Appl. Phys.* **2017**, *122*, 234902. [CrossRef]
51. Fuentes-Domínguez, R.; Yao, M.; Colombi, A.; Dryburgh, P.; Pieris, D.; Jackson-Crisp, A.; Colquitt, D.; Clare, A.; Smith, R.J.; Clark, M. Design of a Resonant Luneburg Lens for Surface Acoustic Waves. *Ultrasonics* **2021**, *111*, 106306. [CrossRef] [PubMed]
52. Legrand, F.; Gérardin, B.; Bruno, F.; Laurent, J.; Lemoult, F.; Prada, C.; Aubry, A. Cloaking, Trapping and Superlensing of Lamb Waves with Negative Refraction. *Sci. Rep.* **2021**, *11*, 23901. [CrossRef] [PubMed]
53. Wang, T.; Song, G.; Wang, Z.; Li, Y. Proof-of-Concept Study of Monitoring Bolt Connection Status Using a Piezoelectric Based Active Sensing Method. *Smart Mater. Struct.* **2013**, *22*, 087001. [CrossRef]
54. Miao, R.; Shen, R.; Zhang, S.; Xue, S. A Review of Bolt Tightening Force Measurement and Loosening Detection. *Sensors* **2020**, *20*, 3165. [CrossRef] [PubMed]
55. Huang, J.; Liu, J.; Gong, H.; Deng, X. A Comprehensive Review of Loosening Detection Methods for Threaded Fasteners. *Mech. Syst. Signal Proc.* **2022**, *168*, 108652. [CrossRef]
56. Yan, G.; Raetz, S.; Chigarev, N.; Blondeau, J.; Gusev, V.E.; Tournat, V. Cumulative Fatigue Damage in Thin Aluminum Films Evaluated Non-Destructively with Lasers via Zero-Group-Velocity Lamb Modes. *NDT E Int.* **2020**, *116*, 102323. [CrossRef]
57. Hodé, R.; Raetz, S.; Blondeau, J.; Chigarev, N.; Cuvillier, N.; Tournat, V.; Ducousso, M. Nondestructive Evaluation of Structural Adhesive Bonding Using the Attenuation of Zero-Group-Velocity Lamb Modes. *Appl. Phys. Lett.* **2020**, *116*, 104101. [CrossRef]
58. Mevissen, F.; Meo, M. A Nonlinear Ultrasonic Modulation Method for Crack Detection in Turbine Blades. *Aerospace* **2020**, *7*, 72. [CrossRef]

59. Williams, W.B.; Michaels, T.E.; Michaels, J.E. Characterization of Guided Wave Velocity and Attenuation in Anisotropic Materials from Wavefield Measurements. *AIP Conf. Proc.* **2016**, *1706*, 030002. [CrossRef]
60. Achenbach, J.D. *Reciprocity in Elastodynamics*; Cambridge Monographs on Mechanics; Cambridge University Press: Cambridge, UK, 2004; ISBN 978-0-521-81734-9.